Lenticular Hexagon-to-Hexagram Shape Transformation: Nano-Origami in Liquid Droplets

Catherine Quilliet,[1,*] Alexander V. Butenko,[2,3] and Eli Sloutskin[3,2,†]

[1] *CNRS/Université Grenoble-Alpes, LIPhy UMR 5588, Grenoble F-38401, France*
[2] *Bar-Ilan Institute of Nanotechnology & Advanced Materials, Bar-Ilan University, Ramat-Gan 5290002, Israel*
[3] *Physics Department, Bar-Ilan University, Ramat-Gan 5290002, Israel*

(Dated: December 8, 2025)

Temperature-controlled droplet shape transformations have been extensively studied, uncovering the mechanism of convex liquid polyhedron formation but failing to account for concave edges. Here, we reveal interfacially-frozen metastable droplets with hexagram projections and concave edges. We combine macroscopic experiments, numerical simulations, and an analytical geometric model, elucidating the mechanism of these phenomena: previously unreported, mobile-fold nano-origami. Our findings open new avenues in self-assembly of complex faceted liquid and solid nanostructures for nanotechnology applications.

Classical, force-free liquid droplets are spherical at equilibrium[1]. However, in the last decade, temperature-controllable self-faceting shape transformations have been discovered in surfactant-stabilized oil-in-water and water-in-oil emulsions with a wide variety of chemical compositions[2–6]. These counterintuitive transformations, driven by 'interfacial freezing' (IF), crystallization of a ≈ 2 nm-thick surface monolayer of the droplets[7, 8], enable unconventional strategies for synthesis of colloids and nanoparticles[9–11], shed light onto the mysterious mechanisms of morphogenesis[12] and the origin of life[3, 6, 13], and provide a unique probe for the elusive elastic properties of curved quasi-2D crystals[14, 15].

Most reported self-faceting experiments[2, 6] involved quasi-equilibrium cooling of the emulsion, with the spherical droplets undergoing a sphere-to-icosahedron transformation, followed at a slightly lower temperature $T = T_{SE}$ by the flattening of the icosahedra into triangular, parallelogram, or hexagonal lenticular shapes with aspect ratios[10, 14] reaching ≈ 10. These shapes, exhibiting only *convex* vertices and edges, are dictated by 'disclination' defects, lattice sites of the IF hexagonal crystal having a coordination number $z = 6-q$, where $q < 6$ is an integer referred to as 'topological charge'[14, 16]. Since the angle between the nearest neighbor bonds of a pristine hexagonal lattice site is $2\pi/6$, a charge-q defect corresponds to an angular deficiency of $(2\pi/6)q$. By classical Euler's topological formula[16–18], the sum of topological charges q over any simply-connected closed surface, such as the IF crystal fully covering a droplet's surface, is precisely 12. Positive charge disclinations promote positive Gaussian curvature, inducing the sphere-to-icosahedron transition, upon which the 12 vertices of the icosahedron, each bearing a topological charge of $q = +1$, buckle out of the spherical surface[19, 20]. The subsequent transformations into the triangular, parallelogram, or hexagonal lenticular shapes involve the coalescence of four, three, or two $q = +1$ defects, respectively, forming the vertices of these shapes. While the outlined-above mechanism was initially subject to some controversy[3, 4, 21], it has been later verified by direct experiments[6, 7, 14, 22].

Remarkably, sporadic observations reported that rapid temperature variation, either reheating[2] or otherwise[23], may induce more complex out-of-equilibrium droplet shapes, where droplet's 2D projection presents a profile with concave apices. In view of the previously studied conformations—where convex apices in a profile indicated convex vertices in the droplet shape—one may wonder if a concave apex in the profile suggests the presence of non-convex vertices in the droplet shape. In particular, this could indicate the existence of negative-q defects, which would correspond, at least locally, to a negative Gaussian curvature[16, 24]. Importantly, on a closed surface the generation of such defects must be precisely compensated by a similar amount of extra positive charge, to avoid Euler's topological formula violation[16, 17]. Yet, in the absence of systematic experiments, the evidence for the extra positive charge could not be tested and the physical mechanism behind the formation of concave apices in the observed profiles remained unknown.

Here we demonstrate lenticular hexagon-to-hexagram droplet profile transformations, with concave apices reproducibly formed by a well-defined temperature variation protocol. We fully resolve the mechanism of this transformation, demonstrating it to avoid both the extra positive topological charge generation and Euler's topological formula violation. In contrast to previously reported self-faceting mechanisms[2, 4, 6, 11, 14], the present transformation involves no splitting or displacement of topological charges — processes that necessarily require mediation by dislocations[25]. Instead, this transformation is driven by spontaneous origami-like folding of the droplet's surface, which we reproduce employing a macroscopic experimental model, a simple analytical model, and computer simulations.

To form the self-faceting emulsion, we suspend by magnetic stirring the oil [hexadecane, $CH_3(CH_2)_{14}CH_3$] in a

* Catherine.Quilliet@univ-grenoble-alpes.fr
† Eli.Sloutskin@biu.ac.il

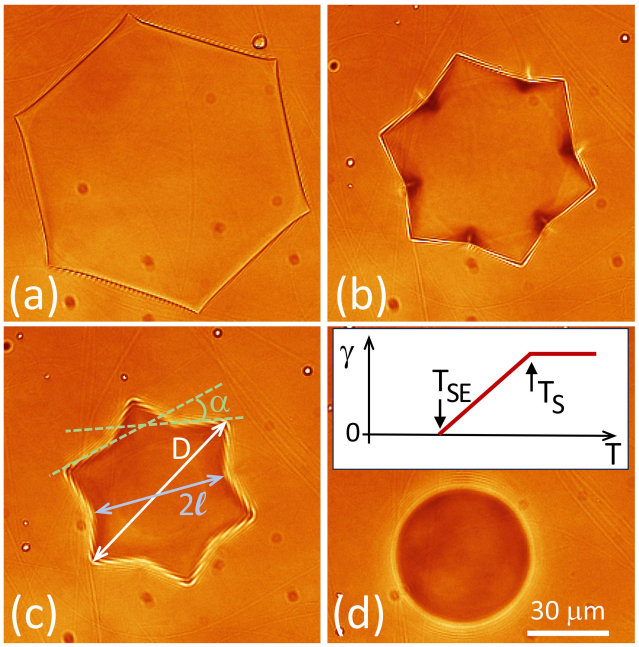

FIG. 1. Bright-field microscopy images of a lenticular hexagonal droplet (a) transforming on heating into a hexagram (b), evolving into (c), and eventually transforming into a spherical droplet (d). Note the lateral contraction of the droplet [the scale bar is shown in (d)]. Note also the folds halfway between the convex vertices in (b), scattering light roughly along the radial direction. The definitions of D, $2l$, and α (see main text) are shown in (c). The inset to (d) shows the schematic temperature-dependence of the droplets' interfacial tension, $\gamma(T)$, exhibiting a near-zero (negative) slope above the interfacial freezing temperature T_s, a high positive slope at $T < T_s$, and vanishing of the interfacial tension at $T = T_{SE}$, where the icosahedra distort into polygonal lenticular shapes. 'Glow' LUT is applied for better visibility of the microscopy images.

1 mM aqueous surfactant [octadecyltrimethylammonium bromide, $CH_3(CH_2)_{17}(CH_3)_3NBr$] solution (1-2% o/w), as described in detail elsewhere[2]. Although many oil-surfactant combinations exhibit self-faceting[5, 8, 21, 23, 26] at surfactant concentrations near or above the critical micelle concentration (CMC)[5], we focus on this particular system because it is well characterized and conveniently exhibits transition temperatures close to room temperature. The emulsion is loaded by capillarity into a $0.1 \times 2 \times 50$ mm Vitrocom™ borosilicate glass capillary, sealed by an instant epoxy glue, and glued wide face down onto a brass platelet. The platelet is then mounted on a temperature-controlled baseplate for bright field microscopy using an inverted Nikon TiE setup equipped with dry Plan Apo 20× ($NA = 0.75$) and Plan Fluor 100× ($NA = 0.9$) objectives, and a Nikon DS-Fi1 CCD camera for video acquisition[2, 8].

To observe the droplet shape transformations, we cool the emulsion droplets (spherical-state radii $\approx 10 - 45$ μm) quasistatically (0.1-0.4°C/min) from ≈ 28°C, where the droplets are perfectly spherical, through the sphere-to-icosahedron transition, down to $T_{SE} \approx 20$°C, where the icosahedra flatten, forming the laterally-expanding polygonal lenticular shapes. Once the transition is detected by optical microscopy, we immediately stop the cooling scan ~~, wait 2-10 min for full temperature equilibration,~~ and focus on one of the lenticular hexagons (Fig. 1(a)). Next, we *increase* the temperature very slowly ($\approx$ 0.1°C/min), which induces lateral contraction of the hexagonal droplet. Strikingly, the contraction is accompanied by the fascinating hexagon-to-hexagram shape transformation, followed by hexagram-to-sphere transformation [see Fig. 1 and Video S1 in Supplementary Information (SI) [27]]. A similar transformation is also observed for other oil-surfactant combinations that exhibit self-faceting (see SI, Section I). Faster heating ($\approx$ 1°C/min) limits shape relaxation and yields slightly distorted hexagrams.

The observed shape transformations are governed by the interplay between the droplet interfacial tension and the elasticity of the interfacial crystalline monolayer. Notably, the 2D Young's modulus Y of the interfacial crystal was previously estimated[2, 7, 19] to lie within $0.6 < Y < 80$ mN/m, comparable to the values reported for *liquid* alkane-surfactant interfacial monolayers[28] ($1 < Y < 18$ mN/m) and unilamellar phospholipid vesicles[29] ($50 < Y < 300$ mN/m). However, vesicles and emulsion droplets whose surfaces are 2D-liquid have a zero shear modulus and therefore do not exhibit self-faceting transitions. Although certain non-spherical shapes have recently been reported for emulsion droplets without IF[30], these shapes are not faceted. Faceting and other shape transformations also occur in droplets of *anisotropic bulk* phases[31–33], where *bulk* elasticity contributes to the deformations, in contrast to the transitions studied here, which are driven by the crystallinity of the interfacial layer.

To understand the origin of lateral expansion and contraction of polygonal droplets upon cooling and heating, respectively, note that the interfacial tension γ exhibits a non-monotonic dependence on temperature. In particular, while $\gamma(T)$ exhibits a near-zero negative slope above the interfacial freezing transition temperature $T_s \approx 26$°C, the slope is high and positive at $T < T_s$, leading to vanishing of γ at $T = T_{SE}$ (inset to Fig. 1(d)). This behavior, reflecting the loss of the interfacial entropy[34, 35] at $T = T_s$, is a well-known signature of the interfacial freezing effect, verified in numerous studies of interfacial freezing, at bulk interfaces[5] and at the surfaces of emulsion droplets[2, 19, 35]. On rapid cooling below T_{SE}, γ transiently turns negative, promoting the increase of the surface area A of the droplets and leading to complex non-equilibrium phenomena[15, 36]. Importantly, our capillary-contained oil-in-water emulsion droplets are compressed by buoyancy against the top of the containing capillary. This compression is negligible for the present droplet sizes, except for in the close vicinity of T_{SE}, where γ is ultralow, allowing the buoyancy to significantly flat-

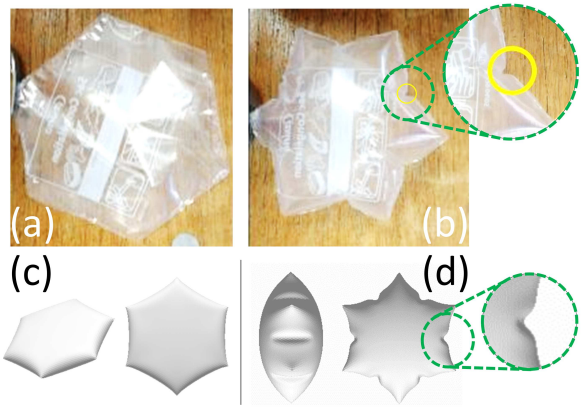

FIG. 2. (a) A macroscopic hexapita model undergoing a shape transformation into a lenticular hexagram (b) upon inflation. The edge length of the hexagon is ≈ 4 cm. (c)-(d) Numerical Surface Evolver simulations of hexapita inflation: (c) after a very slight inflation ($d^\star = 0.01$, $\nu_{2D} = 0.5$, $v = 0.656$); (d) after significant inflation ($d^\star = 0.01$, $\nu_{2d} = 0.5$, $v = 0.84$). Each of panels (c) and (d) presents two views of the simulated shape. Note the similarity in the appearance of the folds forming between the vertices in both macroscopic experiments (encircled in yellow in the inset of (b)) and numerical simulations (inset to (d)); see SI [27] for a quantitative comparison of these folds' geometry. Similar folds also appear in microscopy images of the emulsion droplets (Fig. 1(b)).

ten the droplets[14]. This flattening appears in bright-field microscopy videos as lateral expansion on cooling. Conversely, heating the droplets away from T_{SE} increases the γ value and decreases A, so that the droplets deflatten, appearing to undergo contraction. Since the volume of each droplet V is conserved, with the thermal expansion over this narrow T range being negligible, the droplet's contrast in microscopy images increases upon the deflattening (notice the gradual change of contrast from Fig. 1(a) to (d)).

To describe the geometry of the observed shapes by a single parameter, we adopt the 'compacity': $c = 6\pi^{1/2}VA^{-3/2}$. The compacity is essentially a dimensionless volume, which equals 1 for a perfect sphere and tends to 0 for a flat object. We hypothesize that the hexagon-to-hexagram transition, induced by the γ-controlled contraction of A, is governed solely by the corresponding change in c, together with the presence of the six $q = +2$ topological charges located at the vertices of the initial lenticular hexagon. Guided by this hypothesis,~~description,~~ we reproduce the observed shapes by a simple macroscopic experimental model. In this model, we increase c by the inflation of V, so that the shape transformations conveniently occur at a constant A, rather than at a constant V (and decreasing A) as in the emulsions. In particular, we glue two hexagonal plastic sheets along the edges, forming a closed surface, referred as 'hexapita' (an hexagonal version of the well-known Mediterranean round bread with a hollow, pocket-like interior, known as a 'pita') (Fig. 2(a)). Note, that the angular deficiency at each of hexapita's vertices is $2\pi/3$, corresponding to a topological charge of $q = +2$, as in the experimental hexagonal droplet; q is zero everywhere else. To control the internal volume of our hexapita, we poke a small hole and flow air inside[37], inflating the space enclosed by the two hexagonal plastic sheets. Strikingly, the shape produced by the inflation of our hexapita almost perfectly matches the one observed in emulsion experiments (cf Fig.2(b) and Fig.1(b)). Furthermore, a closer examination reveals the folds formed half-way between the vertices (blown-up in the inset to Fig. 2(b)), similar to the ones occurring in the emulsion droplets (Fig. 1(b)). Notably, the angular deficiency at the vertices of the hexapita does not change during this transformation: the transformation occurs by simple folding, rather than by cutting and gluing. The successful macroscopic reproduction of the hexagon-to-hexagram transition supports our hypothesis that the transformation is governed by compacity together with the fixed locations of the topological defects. Under these conditions, the same mechanism should operate in closed elastic shells of either microscopic or macroscopic size, provided that bending is far less costly than stretching, a regime that is quantified below.

Our successful *qualitative* reproduction of the hexagon-to-hexagram shape transformation by macroscopic hexapita experiments, motivates the construction of an even simpler geometrical model, aiming at a *quantitative* description of this phenomenon. Similarly to the macroscopic experiments, this model assumes the $q = +2$ charges to remain fixed at the vertices of the initially-flat hexapita. In addition, the shape is assumed to maintain the 6-fold symmetry about the z axis, with the (slight) bending, stretch and shear of the facets neglected, so that only linear origami folds are permitted (green dashed lines in Fig. 3(a)). In this purely 3D deformation mode (i.e., without in-plane deformation of the surface), vertical creases emerge midway between the vertices (orange dashes in Fig. 3(a)), forming the folds shown as vertical (i.e. z-parallel) blue lines in Fig. 3(c). The folded 3D shape has flat hexagons as its top and bottom, both rotated by $\pi/6$ relative to the initial flat hexagonal pocket. The shape's edges are capped by six rectangular-based pyramids, oriented horizontally (Fig. 3). For a given value of either the edge a or the apothem R of the initial hexagonal pocket, the inflated shape is fully determined by the choice of ℓ (Fig. 3(d)-(g)). Conversely, the angle α (defined in Fig. 3(b)) unequivocally determines the ratio $D/2\ell$ (see SI [27]):

$$\frac{D}{2\ell} = \frac{\sqrt{3}}{2} + \frac{1}{2}\tan\left(\frac{\pi}{3} - \frac{\alpha}{2}\right), \qquad (1)$$

allowing the model to be tested by a direct, quantitative, scale-free, comparison with emulsion experiments.

To identify the mechanism driving the hexagon-to-hexagram transitions in emulsions, we first quantitatively characterize the shape of the experimental liquid hexagrams by their $D/2\ell$ and α (Fig. 1(c)), measured by

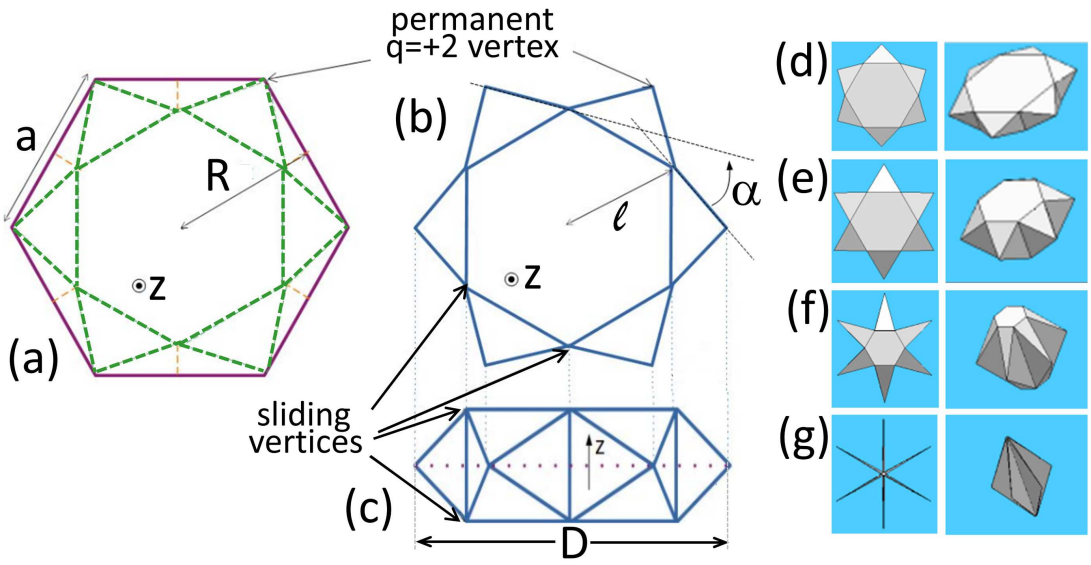

FIG. 3. (a) A flat hexagonal pocket folds along the green dashes, forming creases along the orange dashes, resulting in a 3D shape. (b) and (c) show its top and side views, respectively. Note the z-axis orientation. (d)–(g) display 3D renderings for $\ell^\star \equiv \ell/R = 0.8, 0.6, 0.3$, and 0.02. The parameters α and D, defined in (b) and (c), are fully determined by ℓ and the initial hexagon edge a.

direct microscopy. Strikingly, the resulting values for several different samples overlap (Fig. 4(a)). Furthermore, note the perfect match between the experiments and Eq. (1), derived from our very simple origami model, with no adjustable parameters (Fig. 4(a)). This agreement strongly supports the validity of the central assumption of our origami model[38]: that the topological charges remain fixed at the tips of the vertices, with no generation, annihilation, or displacement of the charges. Remarkably, the location and length of the folds do not arise from a fixed, prescribed design — as is typically the case in origami[39] — but instead continuously evolve. Indeed, the folds 'slide' across the 2D crystal during the evolution of ℓ, as illustrated in Fig. 3 and detailed in the SI calculations[27]: the non-trivial pattern formed by the folds depends uniquely on a single global control parameter — the ~~reduced volume~~ compacity.

As an additional test of our origami model's validity, we use it to analytically calculate the droplet's surface area A and compare it to the experiment. We first define $\ell^\star \equiv \ell/R$ and obtain: $\ell^\star = (2/3^{1/2})\cos(\pi/3 - \alpha/2)$ and $R = D[3^{1/2}\ell^* + (4/3 - \ell^{*2})^{1/2}]^{-1}$, allowing us to compute $A = 4\sqrt{3}R^2$ for any given combination of D and α (see SI [27]). We measure D and α from our experimental microscopy images, substitute them into the expressions for $\ell^\star$ and R, and extract the model prediction for A. The results, obtained in heating scans for three different samples, demonstrate that A decreases (open symbols in Fig. 4(b)), as expected from the temperature-induced *in*crease of γ in the range $T_{SE} < T < T_s$ (inset to Fig. 1(d)).

While measuring the surface area of inflated 3D hexagram droplets is challenging with conventional bright-field microscopy, our experiments provide an accurate measurement of A in two limiting cases: (a) very thin droplets observed near T_{SE}; (b) spherical droplets formed upon heating of the hexagrams. For thin droplets, A is approximately twice their projected area in the x-y plane, A_p, as measured by bright-field microscopy. Remarkably, the surface areas of the thin droplets thus obtained, smoothly converge to the ones predicted by the origami model (compare open symbols and crosses in Fig. 4(b)). For the spherical droplets, $A = 4\pi r^2$, where r is the droplet radius measured by microscopy. Once again, these values (solid symbols in Fig. 4(b)) follow the temperature trend of the origami model predictions (open symbols). These results strongly support the validity of our origami model, justifying the assumptions underlying its foundations. With that, notably, our origami hexapita has zero volume for a perfectly hexagonal shape (i.e., $\alpha = 60°$); consequently, the *volumes* predicted by this very simple model are invalid.

To address the limitations of the origami model, while preserving its most important physical assumptions, we perform finite elements numerical simulations of a hexapita with a stretchable, smoothly bendable surface using the Surface Evolver software[40]. Adopting the thin sheet description of the surface-covering interfacial crystal, we assign it the elastic parameters κ, Y, and ν_{2D}, representing the bending modulus, the 2D Young's modulus, and the Poisson's ratio, respectively[41]. With the droplet volume set to a prescribed value, the elastic energy of the interface is minimized by adjusting its shape and strain (see SI [27]). As in our origami and experiments, six topological charges ($q = +2$) reside at the vertices of the simulated hexapita, dictating the lo-

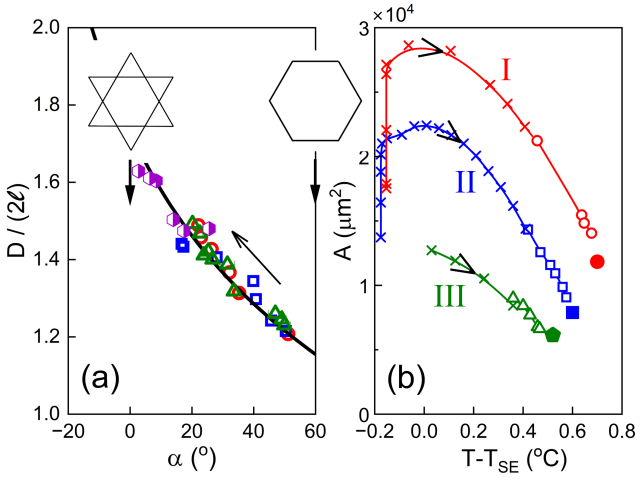

FIG. 4. (a) The mutual dependence between the dimensionless shape descriptors, $D/2\ell$ and α, obtained from emulsion experiments (open symbols), closely matches the predictions of the simple theoretical origami model (Eq. (1); solid curve) and numerical elasticity calculations (half-filled symbols). Note that α is 60° for a perfect hexagon and 0° for a regular (i.e., simple) hexagram, as shown on top. The tilted arrow indicates the time evolution of α and $D/2\ell$ during heating scan experiments, where the hexagon-to-hexagram transition occurs. Statistical measurement errors are smaller than the symbols. (b) Microscopy-measured surface areas A of thin droplets (crosses) and spherical droplets (closed symbols) smoothly follow the trend predicted by the origami model, based on experimentally measured D and α (open symbols). Data from three different samples (denoted by Roman numerals) are shown in different colors, with the same colors and symbols used in both (a) and (b). The curves serve as a guide to the eye. Arrows indicate the time direction in these heating scans. At $T < T_{SE}$, A increases with time at a constant T, as γ is transiently negative[2, 7, 11, 15, 35].

cations of the tips where Gaussian curvature is concentrated. Note that the dimensionless shape descriptors, such as $D/2\ell$ and α, depend only on: (i) the dimensionless volume: $v = 3^{1/4}\pi^{1/2}V/(4R^3)$ (equal to compacity c, when the area does not change), with R defined in Fig. 3(a); (ii) ν_{2D}; (iii) $d^\star = [12(1-\nu_{2D}^2)\kappa/Y]^{1/2}R^{-1}$. For a hypothetical interfacial crystal with isotropic elastic properties, $d^\star$ is the crystal's thickness, divided by R for non-dimensionalization. However, the interface-normal and tangential elastic properties of interfacially-frozen monolayers differ, primarily due to the anisotropic nature of the constituent elongated molecules and their locally parallel alignment within the layer, so $d^\star$ does not have a simple geometrical interpretation, but provides the elastic scale for the deformations[42–44].

In hexapitas with $d^\star \geq 0.03$, the initial hexagon expands continuously upon volume inflation, without undergoing the hexagon-to-hexagram transformation (see SI [27]). However, for $d^\star \leq 0.02$, the inflation generates folds halfway between the vertices, which form through a sudden buckling[41] transition. These folds impart a hexagram shape to the droplet (Fig. 2(c)-(d)). Both the shape and the accompanying folds strongly resemble those observed in our macroscopic experiments (Fig. 2(b)), as well as in the emulsions (Fig. 1(b)). For a quantitative comparison of the simulated shapes to experiments, we measure the simulated values of $D/2\ell$ and α (see SI [27]). Strikingly, the resulting dependence of $D/2\ell$ on α (purple half-filled symbols in Fig. 4(a)) perfectly matches both the experimental observations of emulsion droplets (open symbols) and the analytical dependence derived for the origami model (Eq. (1); solid curve). This agreement strongly supports the proposed mechanism of the hexagon-to-hexagram transitions.

In conclusion, we demonstrate that interfacially frozen oil-in-water emulsion droplets, which spontaneously adopt a lenticular hexagonal shape upon cooling while retaining a liquid bulk, undergo a hexagon-to-hexagram transformation upon heating. This transformation is successfully reproduced by both a simple analytical origami model and numerical simulations. The deformation proceeds via interface folding, which induces both concave and convex edges. Both types of edges occur, and possibly meet, without the generation, annihilation, or displacement of topological charges. This mechanism may have broader implications for morphogenesis, where thin crystalline shells can develop both concave and convex edges to facilitate protein recruitment and other crucial biological processes[6, 45–47]. Beyond biological relevance, our findings suggest a new route for designing complex-shaped colloidal particles[6]. Importantly, since self-faceting transitions are observed even for nanometer-scale droplets[7], this approach may also find applications in nanotechnology, paving the way for advanced self-assembled metamaterials[48, 49] with tunable properties[50].

ACKNOWLEDGMENTS

We thank M. Deutsch and S. Guttman for insightful discussions and technical assistance, and K. Brakke - for developing and maintaining the Surface Evolver software. This research is supported by the Israel Science Foundation (grant no. 2205/21 (E.S.)).

[1] J. D. Paulsen, V. Démery, C. D. Santangelo, T. P. Russell, B. Davidovitch, and N. Menon, Nature Mater. **14**, 1206 1209 (2015).
[2] S. Guttman, Z. Sapir, M. Schultz, A. V. Butenko, B. M. Ocko, M. Deutsch, and E. Sloutskin, Proc. Natl. Acad. Sci. U.S.A. **113**, 493 (2016).
[3] N. Denkov, S. Tcholakova, I. Lesov, D. Cholakova, and S. K. Smoukov, Nature **528**, 392 (2015).

[4] P. A. Haas, D. Cholakova, N. Denkov, R. E. Goldstein, and S. K. Smoukov, Phys. Rev. Research **1**, 023017 (2019).

[5] E. Sloutskin, C. D. Bain, B. M. Ocko, and M. Deutsch, Faraday Discuss. **129**, 339 (2005).

[6] O. Marin, M. Tkachev, E. Sloutskin, and M. Deutsch, Curr. Opin. Colloid Interface Sci. **49**, 107 (2020).

[7] S. Guttman, E. Kesselman, A. Jacob, O. Marin, D. Danino, M. Deutsch, and E. Sloutskin, Nano Lett. **19**, 3161 (2019).

[8] S. Hacmon, S. R. Liber, L. Shool, A. V. Butenko, A. Atkins, and E. Sloutskin, Small **19**, 2301637 (2023).

[9] I. Lesov, Z. Valkova, E. Vassileva, G. S. Georgiev, K. Ruseva, M. Simeonov, S. Tcholakova, N. D. Denkov, and S. K. Smoukov, Macromolecules **51**, 7456 (2018), https://doi.org/10.1021/acs.macromol.8b00529.

[10] O. Marin, M. Alesker, S. Guttman, G. Gershinsky, E. Edri, H. Shpaisman, R. E. Guerra, D. Zitoun, M. Deutsch, and E. Sloutskin, J. Colloid Interf. Sci. **538**, 541 (2019).

[11] A. V. Butenko, E. Hsu, D. A. Matoz-Fernandez, L. Shool, A. B. Schofield, D. Lee, and E. Sloutskin, ACS Nano **19**, 7793 (2025), pMID: 39964250, https://doi.org/10.1021/acsnano.4c13476.

[12] Y. Ravichandran, M. Vogg, K. Kruse, D. J. G. Pearce, and A. Roux, Science Advances **11**, eadr9855 (2025), https://www.science.org/doi/pdf/10.1126/sciadv.adr9855.

[13] R. Gordon, M. M. Hanczyc, N. D. Denkov, M. A. Tiffany, and S. K. Smoukov, *Habitability of the Universe Before Earth*, Emergence of polygonal shapes in oil droplets and living cells: the potential role of tensegrity in the origin of life (Academic Press, 2018) pp. 427–490.

[14] I. García-Aguilar, P. Fonda, E. Sloutskin, and L. Giomi, Phys. Rev. Lett. **126**, 038001 (2021).

[15] E. Hsu, D. Lee, and E. Sloutskin, Nano Lett. **24**, 8717 (2024), pMID: 38976791, https://doi.org/10.1021/acs.nanolett.4c02075.

[16] M. J. Bowick and L. Giomi, Advances in Physics **58**, 449 (2009), https://doi.org/10.1080/00018730903043166.

[17] H. S. M. Coxeter, *The Beauty of Geometry: Twelve Essays* (Dover Publications, Mineola, NY, USA, 1999).

[18] R. E. Guerra, C. P. Kelleher, A. D. Hollingsworth, and P. M. Chaikin, Nature **554**, 346 (2018).

[19] S. Das, A. V. Butenko, Y. Mastai, M. Deutsch, and E. Sloutskin, Nature Physics **18**, 1177 (2022).

[20] S. Davidyan, D. A. Matoz-Fernandez, A. V. Butenko, I. García-Aguilar, L. Giomi, and E. Sloutskin, Phys. Rev. Res. **6**, 043098 (2024).

[21] D. Cholakova, N. Denkov, S. Tcholakova, I. Lesov, and S. K. Smoukov, Adv. Coll. Interf. Sci. **235**, 90 (2016).

[22] S. R. Liber, O. Marin, A. V. Butenko, R. Ron, L. Shool, A. Salomon, M. Deutsch, and E. Sloutskin, J. Am. Chem. Soc. **142**, 8672 (2020), pMID: 32307985, https://doi.org/10.1021/jacs.0c00184.

[23] D. Cholakova and N. Denkov, Advances in Colloid and Interface Science **269**, 7 (2019).

[24] Z. Yao, M. Bowick, X. Ma, and R. Sknepnek, Europhysics Letters **101**, 44007 (2013).

[25] C. Negri, A. L. Sellerio, S. Zapperi, and M. C. Miguel, Proceedings of the National Academy of Sciences **112**, 14545 (2015), https://www.pnas.org/doi/pdf/10.1073/pnas.1518258112.

[26] S. R. Liber, A. V. Butenko, M. Caspi, S. Guttman, M. Schultz, A. B. Schofield, M. Deutsch, and E. Sloutskin, Langmuir **35**, 13053 (2019).

[27] See Supplemental Material at URL-will-be-inserted-by-publisher for the details of experiments with other oil-surfactant combinations, analytical and numerical calculations, fold size and shape descriptor measurements, and experimental video.

[28] D. Georgieva, V. Schmitt, F. Leal-Calderon, and D. Langevin, Langmuir **25**, 5565 (2009), https://doi.org/10.1021/la804240e.

[29] C. A. Rutkowski, L. M. Williams, T. H. Haines, and H. Z. Cummins, Biochemistry **30**, 5688 (1991), pMID: 2043611, https://doi.org/10.1021/bi00237a008.

[30] J. Abacousnac, W. Chen, J. Brujic, and D. G. Grier, Phys. Rev. Res. **7**, 033010 (2025).

[31] K. Peddireddy, S. Copar, K. V. Le, I. Muševic, C. Bahr, and V. S. R. Jampani, Proc. Natl. Acad. Sci. U.S.A. **118**, e2011174118 (2021), https://www.pnas.org/doi/pdf/10.1073/pnas.2011174118.

[32] T. Gibaud, E. Barry, M. J. Zakhary, M. Henglin, A. Ward, Y. Yang, C. Berciu, R. Oldenbourg, M. F. Hagan, D. Nicastro, R. B. Meyer, and Z. Dogic, Nature **481**, 348 (2012).

[33] W.-S. Wei, Y. Xia, S. Ettinger, S. Yang, and A. G. Yodh, Nature **576**, 433 (2019).

[34] X. Z. Wu, B. M. Ocko, E. B. Sirota, S. K. Sinha, M. Deutsch, G. H. Cao, and M. W. Kim, Science **261**, 1018 (1993).

[35] S. Guttman, Z. Sapir, B. M. Ocko, M. Deutsch, and E. Sloutskin, Langmuir **33**, 1305 (2017).

[36] L. Shool, A. V. Butenko, S. R. Liber, Y. Rabin, and E. Sloutskin, J. Phys. Chem. Lett. **12**, 6834 (2021), pMID: 34279944, https://doi.org/10.1021/acs.jpclett.1c01937.

[37] G. Coupier, A. Djellouli, and C. Quilliet, Eur. Phys. J. E **42**, 129 (2019).

[38] J. L. Silverberg, A. A. Evans, L. McLeod, R. C. Hayward, T. Hull, C. D. Santangelo, and I. Cohen, Science **345**, 647 (2014), https://www.science.org/doi/pdf/10.1126/science.1252876.

[39] D. Melancon, B. Gorissen, C. J. García-Mora, C. Hoberman, and K. Bertoldi, Nature **592**, 545 (2021).

[40] K. A. Brakke, Exp. Math. **1**, 141 (1992).

[41] J. Fierling, A. John, B. Delorme, A. Torzynski, G. B. Blanchard, C. M. Lye, A. Popkova, G. Malandain, B. Sanson, J. Étienne, P. Marmottant, C. Quilliet, and M. Rauzi, Nat. Commun. **13**, 3348 (2022).

[42] C. Quilliet, A. Farutin, and P. Marmottant, Eur. Phys. J. E **39**, 58 (2016).

[43] G. Chabouh, B. Dollet, C. Quilliet, and G. Coupier, J. Acoust. Soc. Am. **149**, 1240 (2021).

[44] F. Quéméneur, C. Quilliet, M. Faivre, A. Viallat, and B. Pépin-Donat, Phys. Rev. Lett. **108**, 108303 (2012).

[45] L. A. Hoffmann, L. N. Carenza, J. Eckert, and L. Giomi, Sci. Adv. **8**, eabk2712 (2022), https://www.science.org/doi/pdf/10.1126/sciadv.abk2712.

[46] P. Hirsch and H. Schlesner, "The genus stella," in *The Prokaryotes: A Handbook on Habitats, Isolation, and Identification of Bacteria*, edited by M. P. Starr, H. Stolp, H. G. Trüper, A. Balows, and H. G. Schlegel (Springer Berlin Heidelberg, Berlin, Heidelberg, 1981) pp. 461–465.

[47] L. V. Vasilyeva, Int. J. Syst. Evol. Microbiol. **35**, 518 (1985).

[48] K. Bertoldi, V. Vitelli, J. Christensen, and M. van Hecke, Nat. Rev. Mater. **2**, 17066 (2017).

[49] E. Siéfert, E. Reyssat, J. Bico, and B. Roman, Nat. Mater. **18**, 24 (2019).
[50] A. Rafsanjani, K. Bertoldi, and A. R. Studart, Sci. Robot. **4**, eaav7874 (2019), https://www.science.org/doi/pdf/10.1126/scirobotics.aav7874.
[51] L. D. Landau and E. M. Lifshitz, *Elasticity Theory* (Pergamon, Oxford, 1986).
[52] W. Pietraszkiewicz, Arch. Mech. **26**, 221 (1974).
[53] W. Helfrich, Z. Naturforsch. **C 28**, 693 (1973).